A parametric model for the changes in the complex valued conductivity of a lung during tidal breathing

Sven Nordebo[1], Mariana Dalarsson[1], Davood Khodadad[1], Beat Müller[2], Andreas D. Waldman[2], Tobias Becher[3], Inez Frerichs[3], Louiza Sophocleous[4], Daniel Sjöberg[5], Nima Seifnaraghi[6], Richard Bayford[6]

[1] Department of Physics and Electrical Engineering, Linnæus University, 351 95 Växjö, Sweden. E-mail:
{sven.nordebo,mariana.dalarsson,davood.khodadad}@lnu.se.
[2] Swisstom AG, Schulstrasse 1, 7302 Landquart, Switzerland. E-mail:
{bmu,awa}@swisstom.com
[3] Department of Anaesthesiology and Intensive Care Medicine, University Medical Centre Schleswig-Holstein, Campus Kiel, 24105 Kiel, Germany. E-mail:
{Tobias.Becher,Inez.Frerichs}@uksh.de.
[4] The KIOS Research Center, Department of Electrical and Computer Engineering, University of Cyprus, Nicosia, Cyprus. E-mail:
louiza.sophocleous@gmail.com.
[5] Department of Electrical and Information Technology, Lund University, Box 118, 221 00 Lund, Sweden. E-mail: daniel.sjoberg@eit.lth.se.
[6] Department of Natural Sciences, Middlesex University, Hendon campus, The Burroughs, London, NW4 4BT, United Kingdom. E-mail:
nima.seifnaraghi@gmail.com, R.Bayford@mdx.ac.uk.

Abstract. Classical homogenization theory based on the Hashin-Shtrikman coated ellipsoids is used to model the changes in the complex valued conductivity (or admittivity) of a lung during tidal breathing. Here, the lung is modeled as a two-phase composite material where the alveolar air-filling corresponds to the inclusion phase. The theory predicts a linear relationship between the real and the imaginary parts of the change in the complex valued conductivity of a lung during tidal breathing, and where the loss cotangent of the change is approximately the same as of the effective background conductivity and hence easy to estimate. The theory is illustrated with numerical examples based on realistic parameter values and frequency ranges used with Electrical Impedance Tomography (EIT). The theory may be potentially useful for imaging and clinical evaluations in connection with lung EIT for respiratory management and control.

1. Introduction

Electrical Impedance Tomography (EIT) is a non-radiative, inexpensive technique that can facilitate real time dynamic monitoring of regional lung aeration and ventilation for clinical use [1]. The approach lacks spatial resolution, but it benefits largely from its high temporal resolution and is therefore currently emerging as a technique that can potentially reduce complications and disability in preterm babies by continuous bedside monitoring and respiratory management [2, 3].

From a mathematical/physical point of view, EIT constitutes an ill-posed inverse problem [4–7], and the use of EIT as a successful imaging modality relies therefore on the effectiveness of creating difference conductivity images rather than to generate absolute reconstructions, see *e.g.*, [8, 9]. The difference imaging approach benefits from the linearization of the forward problem, and it alleviates much of the sensitivity to sensor imperfections as well as the unknown background parameter values. In lung EIT, tidal images can be created by using a breath detector [10] providing difference voltage data that is perfectly synchronized with the time of end-expiration and end-inspiration, defining the breathing cycle. For these tidal images, EIT related lung function parameters such as Center of Ventilation, Silent Spaces and ventilation distribution, etc., can then be calculated [3].

Early EIT systems were usually designed for operation at very low frequencies, typically in the kilohertz range [11, 12], where the conductivity of biological tissue usually is considered to be purely resistive (even though this is not entirely true [13]). However, the need of improved image quality in both the spatial and the temporal domains is nowadays driving the development of the commercial EIT systems and their data acquisition hardware to higher speeds (typically in the range of several hundreds of kilohertz) and hence their performance requirements imply that the imaginary part of the complex valued conductivity (or admittivity) of human tissue no longer can be disregarded. Notably, this constitutes a technical challenge, but it can also be a great asset due to the additional clinical information carried by the permittivity of the tissue. To this end, there is no fundamental limitation associated with the reconstruction of the complex valued conductivity using standard optimization algorithms such as in [4, 5, 7, 9, 11], nor with the new developments such as the D-bar methods [14, 15]. In this paper, we investigate a mathematical/physical mechanism that can model the changes in the complex valued conductivity of a lung during tidal breathing. This is particularly interesting as it is already empirically known that the EIT pixel sum of (real valued) conductivity changes within a particular region of interest is almost linearly related to the changes in lung volume, see *e.g.*, [12].

A comprehensive overview on the dielectric spectral properties of biological tissue, including modeling, measurements and literature is given in [13, 16, 17]. In particular, as a realistic estimate of the background conductivity of an inflated lung we have used here the real valued conductivity and permittivity data from [13, Fig. 2e on p. 2257] which is of bovine origin. Measurement data from human tissue, and in particular from neonatal patients is obviously very difficult to obtain. Hence, in order to estimate the typical volume fraction of air during tidal breathing we have used data regarding the lung volume of an adult male and the corresponding condensed matter weight from [18] and [19], respectively.

A basic model predicting the dielectric properties of lung tissue as a function of air content was given in [20], and which has been followed by several other works, see *e.g.*, [21] and [22] with references. The basic work in [20] was followed by a comprehensive study based on EIT spectroscopy measurements and an improved model taking both the air content and tissue dispersion into account [21]. In [22] is given an experimental study of dielectric properties of human lung tissue in vitro and its dependency on the air

filling factor. Human lung tissue specimens from more than 100 patients were investigated with respect to the differences in the impedance spectrum for cancerous and normal tissue, and where the cancerous tissue typically show much larger conductivity values due to the deterioration of the alveolar structure. The same can also be said about interstitial pneumonia [20], where the increased conductivity is explained by the increased thickness of the alveolar walls. Notably, the investigations on the dielectric properties of lung tissue as a function of air content in [20] and [22] are *in vitro*, with volume fractions of air up to about 58-60 %, whereas our estimates of the air content with reference to [18] and [19] are rather in the range 75-78 % for tidal breathing *in vivo*.

The dielectric measurements in [20] were made on the excised lungs of slaughtered calves in the frequency range of 5 kHz to 100 kHz, and a simple theory was developed to model the complex valued conductivity as a function of air filling. The theoretical model in [20] is based on the deformation of a cube-shaped alveolus where the conductivity is given approximately as the conductivity of the enclosing walls of a square cylinder where the volume of the (periodic) wall system is kept fixed and the cube size and the wall thickness are variable to account for the deformation of the epithelial cells and blood vessels through the expansion of the alveoli. The parameters of the model are adjusted by histological investigations. In this way, the thinning of the alveolar walls can explain the decrease of effective conductivity and permittivity of the lung as a function of an increased air filling.

In this paper, we derive an alternative physical model based on classical homogenization theory [23, 24] to predict the changes in the complex valued conductivity of a lung during tidal breathing. The lung is modeled here as a two-phase composite material where the alveolar air-filling corresponds to the inclusion phase and the exterior phase is due to the blood and tissue. The parametric model is based on classical Hashin-Shtrikman/Maxwell-Garnett theory [23, 24] and is simple and well-suited for an analytical study on the changes in the effective conductivity of the lung due to the corresponding small changes in the volume fraction of air during tidal breathing. This model is in many ways similar to that of [20] (an effective conductivity model with thinning of the alveolar walls, etc.), but it has a rigorous foundation in homogenization theory. In particular, the parametric model based on the Hashin-Shtrikman (HS) assemblage [24] comprises a fully three-dimensional homogenization of the lung tissue with ellipsoidal shaped alveoli constituting the inclusion phase. The HS assemblage furthermore accounts for the random nature of the alveolar structure, as seen in *e.g.*, [20, Figs. 14 and 15 on p. 711], by the inherent variation of the HS scaling and positioning of the prototype ellipsoid. Hence, it may be argued from the figures in [20] that the shape of the alveoli is typically more round than square and that the close packing of alveoli at high air content can be achieved due to a large variation in their sizes, similar to the HS assemblage.

The presented parametric model predicts an almost linear relationship between the real and the imaginary parts of the changes in the complex valued conductivity of a lung during tidal breathing, and where the loss cotangent of the change is approximately the same as of the effective background conductivity and hence easy to estimate. It is expected that this a priori knowledge can be useful in the development of new improved image reconstruction algorithms exploiting complex valued measurement data, and/or to define new clinically useful outcome parameters in lung EIT. The theoretical study is based on realistic parameter choices for the conductivity of an inflated lung [13], and hence the corresponding loss cotangent is estimated to be in the order of about $\cot \delta = 0.2$ at 200 kHz. It should be noted that, even at low frequencies, the loss cotangent of the inflated lung may not be negligible (due to the very high relative permittivity of tissue at low frequencies), and is expected to be in the order of about $\cot \delta = 0.1$ at 1 kHz. At higher frequencies, it will increase to about $\cot \delta = 0.3$ at 1 MHz [13]. The theoretical study is illustrated with numerical examples.

2. Homogenization theory based on Hashin-Shtrikman coated ellipsoids

A brief review on the classical homogenization theory based on Hashin-Shtrikman coated ellipsoids is given in this section, see [24] for an in depth derivation of the corresponding results.

2.1. Notation and conventions

The following notation and conventions will be used below. Classical electromagnetic theory is considered based on SI-units [25], and with time convention $e^{j\omega t}$ for time harmonic fields where ω is the angular frequency. Let μ_0, ϵ_0 and c_0 denote the permeability, the permittivity and the speed of light in vacuum, respectively, and where $c_0 = 1/\sqrt{\mu_0 \epsilon_0}$. A passive, homogeneous and isotropic dielectric material with complex valued relative permittivity $\epsilon = \epsilon' - j\epsilon''$ and real valued conductivity $\sigma_r \geq 0$ has complex valued conductivity (or admittivity) σ given by $\sigma = \sigma_R + j\sigma_I$ where $\sigma_I = \omega\epsilon_0\epsilon'$ represents the lossless capacitive part and $\sigma_R = \sigma_r + \omega\epsilon_0\epsilon'' \geq 0$ includes both the conduction and the dielectric losses. The

complex valued conductivity is conveniently written as $\sigma = \sigma_{\mathrm{R}}(1 + \mathrm{j}\eta)$ where $\eta = \cot \delta$ is the loss cotangent (corresponding to the more commonly used loss tangent $\tan \delta = \sigma_{\mathrm{R}}/\sigma_{\mathrm{I}} = 1/\eta$). Both parameters σ_{R} and σ_{I} may depend on frequency, in which case they must also satisfy the associated Kramers-Kronig relations, see *e.g.*, [26, 27]. The cartesian unit vectors are denoted $(\hat{\boldsymbol{x}}_1, \hat{\boldsymbol{x}}_2, \hat{\boldsymbol{x}}_3)$. Finally, the real and imaginary part and the complex conjugate of a complex number ζ are denoted $\Re\{\zeta\}$, $\Im\{\zeta\}$ and ζ^*, respectively.

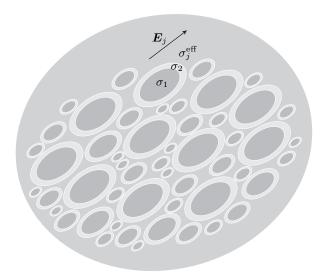## 2.2. The Hashin-Shtrikman coated ellipsoid assemblage

Figure 1. The Hashin-Shtrikman coated ellipsoid assemblage. The figure illustrates a partial assemblage in a process that is completed when all space has been filled with ellipsoids. Here, $\boldsymbol{E}_j$ denotes the applied electric field, σ_j^{eff} the homogenized (effective) conductivity parameter and σ_1 and σ_2 the core and the exterior conductivity of the prototype ellipsoid, respectively.

Consider a general anisotropic two-phase composite material consisting of an inclusion phase with conductivity σ_1 and an exterior phase with conductivity σ_2 and where the volume fraction of the inclusion phase is given by the parameter f. A classical homogenization approach to model such a material is given by the Hashin-Shtrikman coated ellipsoid assemblage [24], as illustrated in figure 1. All the coated ellipsoids are scaled and translated versions of a single prototype coated ellipsoid consisting of a core (inclusion) phase with conductivity σ_1 and an exterior (coating) phase with conductivity σ_2. The semi-axis lengths of the prototype core and exterior ellipsoids are denoted l_{c_j} and l_{e_j}, respectively, and where $j = 1, 2, 3$ refers to the cartesian coordinates x_1, x_2 and x_3, respectively. The prototype core and exterior ellipsoids are confocal in the sense that they can both be represented in the same

system of elliptical coordinates as

$$\frac{x_1^2}{c_1^2 + \rho} + \frac{x_2^2}{c_2^2 + \rho} + \frac{x_3^2}{c_3^2 + \rho} = 1, \tag{1}$$

where c_j are constants and ρ the elliptical coordinate playing the role of the "radius". Hence, with ρ_{c} and ρ_{e} denoting the "radius" of the two confocal ellipsoids, we have

$$\frac{l_{\mathrm{c}_j}^2}{c_j^2 + \rho_{\mathrm{c}}} = \frac{l_{\mathrm{e}_j}^2}{c_j^2 + \rho_{\mathrm{e}}} = 1, \tag{2}$$

which implies that

$$l_{\mathrm{e}_j}^2 = l_{\mathrm{c}_j}^2 + \alpha, \tag{3}$$

where $\alpha = \rho_{\mathrm{e}} - \rho_{\mathrm{c}} > 0$ and $j = 1, 2, 3$. The volume of the two prototype ellipsoids are $V_{\mathrm{c}} = 4\pi l_{\mathrm{c}_1} l_{\mathrm{c}_2} l_{\mathrm{c}_3}/3$ and $V_{\mathrm{e}} = 4\pi l_{\mathrm{e}_1} l_{\mathrm{e}_2} l_{\mathrm{e}_3}/3$, and hence the volume fraction between the core phase and the total volume of the coated ellipsoid is given by

$$f = \frac{V_{\mathrm{c}}}{V_{\mathrm{e}}} = \frac{l_{\mathrm{c}_1} l_{\mathrm{c}_2} l_{\mathrm{c}_3}}{l_{\mathrm{e}_1} l_{\mathrm{e}_2} l_{\mathrm{e}_3}}. \tag{4}$$

The Hashin-Shtrikman coated ellipsoid assemblage is obtained when the whole space is filled with scaled ellipsoids as indicated in figure 1. In this way, the resulting assemblage models the general anisotropic two-phase composite material where the volume fraction f of the inclusion phase is preserved and parameterized according to (4).

2.3. The effective conductivity

Consider a single prototype coated ellipsoid with core and exterior conductivities σ_1 and σ_2, respectively, as described in section 2.2 above. Suppose further that the prototype ellipsoid is embedded in an arbitrary homogeneous auxiliary medium with conductivity σ^{eff}, and excited with an external static electric field $\boldsymbol{E}_j = E_0 \hat{\boldsymbol{x}}_j$ aligned with the jth axis of the ellipsoid, as illustrated in figure 1. The fundamental equations to be solved are given by

$$\begin{cases} \nabla \times \boldsymbol{E}(\boldsymbol{r}) = \boldsymbol{0}, \\ \nabla \cdot \boldsymbol{J}(\boldsymbol{r}) = 0, \\ \boldsymbol{J}(\boldsymbol{r}) = \sigma(\boldsymbol{r})\boldsymbol{E}(\boldsymbol{r}), \end{cases} \tag{5}$$

where $\boldsymbol{E}(\boldsymbol{r})$ and $\boldsymbol{J}(\boldsymbol{r})$ are the electric field intensity and the electric current density, respectively, and where $\sigma(\boldsymbol{r})$ is the complex valued conductivity which is assigned the appropriate constant values $(\sigma_1, \sigma_2, \sigma^{\mathrm{eff}})$ inside and outside the prototype ellipsoid, respectively. The electric field outside the prototype ellipsoid may furthermore be denoted $\boldsymbol{E}(\boldsymbol{r}) = \boldsymbol{E}_j(\boldsymbol{r}) + \boldsymbol{E}_{\mathrm{s}}(\boldsymbol{r})$ where $\boldsymbol{E}_{\mathrm{s}}(\boldsymbol{r})$ may be thought of as the scattered field. The boundary conditions supplementing the equations in (5) are obtained from the continuity of the normal component of the current density $\boldsymbol{J}(\boldsymbol{r})$ at the media

interfaces. The equations in (5) can be solved by introducing the scalar potential $\Phi(\boldsymbol{r})$ where $\boldsymbol{E}(\boldsymbol{r}) = -\nabla\Phi(\boldsymbol{r})$, and where $\Phi(\boldsymbol{r})$ satisfies the Laplace equation $\nabla^2\Phi(\boldsymbol{r}) = 0$, together with the continuity of $\Phi(\boldsymbol{r})$ as well as the continuity of the normal current $\sigma(\boldsymbol{r})\frac{\partial}{\partial n}\Phi(\boldsymbol{r})$ at the media interfaces.

Since the elliptical coordinates constitute one of the very special coordinate systems for which the Laplace operator can be separated [28], the electrostatic problem above can be solved analytically involving ordinary functions and elliptic integrals, see *e.g.*, [24, 28, 29]. In particular, by investigating these analytic solutions, it is found that one can choose the auxiliary medium parameter σ^{eff} in such a way as to render the scattered field $\boldsymbol{E}_{\text{s}}(\boldsymbol{r}) = \boldsymbol{0}$ (and at the same time there is a uniform non-zero field inside the ellipsoid core with the same polarization direction as the applied field). Hence, in this situation the prototype ellipsoid is in some sense cloaked as it does not interfere with the surrounding uniform current field. The resulting auxiliary, or effective, medium parameter σ_j^{eff} depend in general on the polarization direction $\hat{\boldsymbol{x}}_j$, and is given by

$$\sigma_j^{\text{eff}} = \sigma_2 + \frac{f\sigma_2(\sigma_1 - \sigma_2)}{\sigma_2 + \left(d_{\text{c}_j} - fd_{\text{e}_j}\right)(\sigma_1 - \sigma_2)}, \tag{6}$$

where the depolarizing factors (*cf.*, the geometrical factors in [29], and the demagnetizing factors in [30]) d_{c_j} and d_{e_j} are given by $d_{\text{c}_j} = d_j(l_{\text{c}_1}, l_{\text{c}_2}, l_{\text{c}_3})$, $d_{\text{e}_j} = d_j(l_{\text{e}_1}, l_{\text{e}_2}, l_{\text{e}_3})$ where

$$\begin{aligned} &d_j(l_1, l_2, l_3) \\ &= \frac{l_1 l_2 l_3}{2}\int_0^\infty \frac{\mathrm{d}y}{(l_j^2 + y)\sqrt{(l_1^2 + y)(l_2^2 + y)(l_3^2 + y)}}, \end{aligned} \tag{7}$$

and where l_1, l_2 and l_3 are the semi-axis lengths of the corresponding ellipsoids, and $j = 1, 2, 3$, see [24, p. 129]. The depolarizing factors are normalized in the sense that $d_1 + d_2 + d_3 = 1$.

Since further scaled and translated coated ellipsoids can be inserted into the effective medium without disturbing the surrounding uniform current field, the resulting Hashin-Shtrikman coated ellipsoid assemblage can finally be viewed from a macroscopic scale to have the homogeneous and anisotropic constitutive relation

$$\boldsymbol{J} = \boldsymbol{\sigma}^{\text{eff}} \cdot \boldsymbol{E}, \tag{8}$$

where the effective conductivity dyadic $\boldsymbol{\sigma}^{\text{eff}}$ is given by

$$\boldsymbol{\sigma}^{\text{eff}} = \sum_{j=1}^3 \sigma_j^{\text{eff}}\hat{\boldsymbol{x}}_j\hat{\boldsymbol{x}}_j. \tag{9}$$

The coated sphere is a special case of the coated ellipsoid with $d_{\text{c}_j} = d_{\text{e}_j} = 1/3$ for $j = 1, 2, 3$, and hence

$$\sigma_{\text{sph}}^{\text{eff}} = \sigma_2 + \frac{3f\sigma_2(\sigma_1 - \sigma_2)}{3\sigma_2 + (1 - f)(\sigma_1 - \sigma_2)}, \tag{10}$$

which is identical with the classical Maxwell-Garnett mixing formula, see *e.g.*, [23, 24].

2.4. Spheroidal inclusions

Spheroids are particularly simple ellipsoidal shapes having rotational symmetry, and for which the corresponding depolarizing factors as well as their surface areas can be expressed by explicit formulas involving simple functions. Without loss of generality, it will be assumed here that the axis of rotation is defined by the x_1-axis.

A prolate spheroid is characterized by its semi-axis properties $l_1 > l_2 = l_3 = l$, and hence with depolarizing factors $d_1 < d_2 = d_3 = d$ where $d_1 < 1/3$ and $d = (1 - d_1)/2$. The eccentricity of the prolate spheroid is defined by

$$\varepsilon = \sqrt{1 - \left(\frac{l}{l_1}\right)^2}, \tag{11}$$

and the corresponding depolarizing factor d_1 is given by

$$d_1 = \frac{1 - \varepsilon^2}{\varepsilon^2}\left(\frac{1}{2\varepsilon}\ln\left(\frac{1 + \varepsilon}{1 - \varepsilon}\right) - 1\right), \tag{12}$$

cf., *e.g.*, [24, p. 132] and [30, pp. 352–354]. The surface area of the prolate spheroid is furthermore given by

$$S = 2\pi l^2 + 2\pi\frac{ll_1}{\varepsilon}\arcsin\varepsilon, \tag{13}$$

see [31, p. 364].

An oblate spheroid is characterized by its semi-axis properties $l_1 < l_2 = l_3 = l$, and hence with depolarizing factors $d_1 > d_2 = d_3 = d$ where $d_1 > 1/3$ and $d = (1 - d_1)/2$. The eccentricity of the oblate spheroid is defined by

$$\varepsilon = \sqrt{1 - \left(\frac{l_1}{l}\right)^2}, \tag{14}$$

and the corresponding depolarizing factor d_1 is given by

$$d_1 = \frac{1}{\varepsilon^2}\left(1 - \frac{\sqrt{1 - \varepsilon^2}}{\varepsilon}\arcsin\varepsilon\right), \tag{15}$$

cf., *e.g.*, [24, p. 132] and [30, pp. 352–354]. The surface area of the oblate spheroid is furthermore given by

$$S = 2\pi l^2 + \pi\frac{l_1^2}{\varepsilon}\ln\left(\frac{1 + \varepsilon}{1 - \varepsilon}\right), \tag{16}$$

see [31, p. 364].

3. A parametric model for the changes in the conductivity of a lung during tidal breathing

A Hashin-Shtrikman homogenization approach based on (6) is considered to model the changes in the complex valued conductivity of a lung during tidal breathing. The lung is modelled as a two-phase composite material where the air-filled alveoli

constitute the inclusion phase with volume fraction f and conductivity $\sigma_1 = j\omega\epsilon_0$ corresponding to the electric displacement current in vacuum (similar as in air). The conductivity σ_2 of the exterior phase can be identified from some a priori information regarding the effective conductivity σ_{EI} of an inflated lung. Hence, it is assumed that the conductivity of the inflated lung obtained from measurements such as in [13] can be used as an effective conductivity of the lung corresponding to a certain maximum volume fraction f_{EI} at end-inspiration, and where the alveoli have a maximally extended spherical shape. The conductivity of the exterior phase can then be obtained by solving the Maxwell-Garnett equation (10) with respect to σ_2 when the effective parameter $\sigma_{\mathrm{sph}}^{\mathrm{eff}} = \sigma_{\mathrm{EI}}$ is given. This is equivalent to finding the roots of the following second order polynomial equation

$$\sigma_2^2 2\left(1 - f_{\mathrm{EI}}\right) + \sigma_2\left(\sigma_1\left(1 + 2f_{\mathrm{EI}}\right) - \sigma_{\mathrm{EI}}\left(2 + f_{\mathrm{EI}}\right)\right) \\ - \sigma_{\mathrm{EI}}\left(1 - f_{\mathrm{EI}}\right)\sigma_1 = 0, \qquad (17)$$

and where the root of physical interest has $\Re\{\sigma_2\} > 0$ and $\Im\{\sigma_2\} > 0$ (unless the exterior phase is a Drude material with $\Im\{\sigma_2\} < 0$, etc.).

Tidal breathing is then considered with small changes in alveolar air-filling where the corresponding volume fraction f changes from its maximum value f_{EI} at end-inspiration to its minimum value f_{EE} at end-expiration. Two fundamentally different physical modes of alveolar air-fillings are considered for the tidal breathing.

- *Spherical shaped alveoli with fixed shape and varying surface area:* The alveoli are assumed to have a fixed spherical shape and the volume change is obtained by a change of its radius. This implies that the surface area of the alveoli as well as the whole structure of the lung is stretched during the tidal breathing.

- *Spheroidal shaped alveoli with varying shape and fixed surface area:* The alveoli are assumed to have a varying spheroidal shape and the volume change is obtained by a change of its spheroidal eccentricity while keeping its surface area fixed. In this mode, the volume change of the alveoli is due solely to a change in the alveolar shape (prolongation or flattening of the spheroid) with a minor stretch in the lung structure.

With a tidal breathing based on spherical shaped alveoli (fixed shape and varying surface area) the change in conductivity is obtained from (10) as $\Delta\sigma_{\mathrm{sph}}^{\mathrm{eff}} = \sigma_{\mathrm{sph}}^{\mathrm{eff}}(f) - \sigma_{\mathrm{sph}}^{\mathrm{eff}}(f_{\mathrm{EI}})$ where f denotes the volume fraction of air-filled alveoli during tidal breathing and f_{EI} the corresponding value at end-inspiration. Hence

$$\Delta\sigma_{\mathrm{sph}}^{\mathrm{eff}} = \frac{3f\sigma_2\left(\sigma_1 - \sigma_2\right)}{3\sigma_2 + \left(1 - f\right)\left(\sigma_1 - \sigma_2\right)}$$

$$-\frac{3f_{\mathrm{EI}}\sigma_2\left(\sigma_1 - \sigma_2\right)}{3\sigma_2 + \left(1 - f_{\mathrm{EI}}\right)\left(\sigma_1 - \sigma_2\right)}, \qquad (18)$$

where $f = f_{\mathrm{EI}} - \Delta f$ and $\Delta f > 0$. For a comparison with the spheroidal case below, the Hashin-Shtrikman prototype core sphere is defined to have unit radius at maximal volume fraction f_{EI} corresponding to the surface area $S_0 = 4\pi$.

With a tidal breathing based on spheroidal shaped alveoli (varying shape and fixed surface area) the change in conductivity is obtained from (6) and defined by $\Delta\sigma_j^{\mathrm{eff}} = \sigma_j^{\mathrm{eff}}(f) - \sigma_j^{\mathrm{eff}}(f_{\mathrm{EI}})$. The prototype core spheroids are furthermore assumed to be unit spheres at the maximal volume fraction f_{EI} at end-inspiration, and hence from (6) and (10)

$$\Delta\sigma_j^{\mathrm{eff}} = \frac{f\sigma_2\left(\sigma_1 - \sigma_2\right)}{\sigma_2 + \left(d_{\mathrm{c}_j} - fd_{\mathrm{e}_j}\right)\left(\sigma_1 - \sigma_2\right)}$$

$$-\frac{3f_{\mathrm{EI}}\sigma_2\left(\sigma_1 - \sigma_2\right)}{3\sigma_2 + \left(1 - f_{\mathrm{EI}}\right)\left(\sigma_1 - \sigma_2\right)}, \qquad (19)$$

where $f = f_{\mathrm{EI}} - \Delta f$ and $\Delta f > 0$. Here, d_{c_j} and d_{e_j} are the depolarizing factors of the Hashin-Shtrikman prototype core and exterior spheroids at volume fraction f, respectively. Since the Hashin-Shtrikman prototype core spheroid coincides with the unit sphere at maximal volume fraction f_{EI}, the following relation is obtained from (4)

$$f_{\mathrm{EI}} = \frac{1}{l_{\mathrm{e}_1} l_{\mathrm{e}_2} l_{\mathrm{e}_3}}, \qquad (20)$$

where the product $l_{\mathrm{e}_1} l_{\mathrm{e}_2} l_{\mathrm{e}_3}$ is proportional to the volume of the prototype exterior spheroid. Finally, the eccentricity ε of the prototype core spheroid as defined in (11) or (14) is used as a parameter to control the shape of the spheroid, as well as its volume fraction $f < f_{\mathrm{EI}}$.

3.1. The prototype core spheroids

Consider a prolate core spheroid with l_{c_1} being the length of the semi-axis of rotation and $l_{\mathrm{c}} = l_{\mathrm{c}_2} = l_{\mathrm{c}_3}$ the length of the orthogonal axes. Let the spheroidal eccentricity $\epsilon = \sqrt{1 - t^2}$ be fixed, where $t = l_{\mathrm{c}}/l_{\mathrm{c}_1}$, $0 < t < 1$ and $0 < \varepsilon < 1$. The surface area of the prototype core spheroid is fixed at $S = 4\pi$, and hence (13) yields the equation

$$2\pi l_{\mathrm{c}}^2 + 2\pi\frac{l_{\mathrm{c}} l_{\mathrm{c}_1}}{\varepsilon}\arcsin\varepsilon = 4\pi, \qquad (21)$$

and which can be solved for l_{c} to yield

$$l_{\mathrm{c}} = \sqrt{\frac{2\varepsilon t}{\varepsilon t + \arcsin\varepsilon}}, \qquad (22)$$

and $l_{\mathrm{c}_1} = l_{\mathrm{c}}/t$. The corresponding depolarizing factor d_{c_1} is given by (12) and $d_{\mathrm{c}} = (1 - d_{\mathrm{c}_1})/2$.

Consider similarly an oblate core spheroid with l_{c_1} being the length of the semi-axis of rotation and $l_{\mathrm{c}} = l_{\mathrm{c}_2} = l_{\mathrm{c}_3}$ the length of the orthogonal axes. Let

the spheroidal eccentricity $\epsilon = \sqrt{1 - t^2}$ be fixed, where $t = l_{c_1}/l_c$, $0 < t < 1$ and $0 < \varepsilon < 1$. The surface area of the prototype core spheroid is fixed at $S = 4\pi$, and hence (16) yields the equation

$$2\pi l_c^2 + \pi \frac{l_{c_1}^2}{\varepsilon} \ln\left(\frac{1+\varepsilon}{1-\varepsilon}\right) = 4\pi, \tag{23}$$

and which can be solved for l_c to yield

$$l_c = \sqrt{\frac{4\varepsilon}{2\varepsilon + t^2 \ln\left(\frac{1+\varepsilon}{1-\varepsilon}\right)}}, \tag{24}$$

and $l_{c_1} = t l_c$. The corresponding depolarizing factor d_{c_1} is given by (15) and $d_c = (1 - d_{c_1})/2$.

3.2. The prototype external spheroids

By increasing the eccentricity $\varepsilon > 0$ of the prototype core spheroid while keeping its surface area fixed, its volume will decrease. Hence, by defining the volume of the prototype exterior spheroid $V_e = 4\pi l_{e_1} l_{e_2} l_{e_3}/3$ to be fixed, the corresponding volume fraction f of the inclusion phase will decrease. The volume fraction f for a given eccentricity ε is hence obtained from (4) and (20) as

$$f = f_{EI} l_{c_1} l_c^2. \tag{25}$$

To find the semi-axes of the prototype exterior spheroid at volume fraction f, the relations (3) of the confocal ellipsoids are now inserted into the following equation based on the definition (4)

$$f^2 l_{e_1}^2 l_{e_2}^2 l_{e_3}^2 = l_{c_1}^2 l_{c_2}^2 l_{c_3}^2, \tag{26}$$

and which is equivalent to finding the real and positive root of the algebraic equation

$$\alpha^3 + \alpha^2 \left(l_{c_1}^2 + 2l_c^2\right) + \alpha \left(2l_{c_1}^2 l_c^2 + l_c^4\right)$$
$$+ l_{c_1}^2 l_c^4 \left(1 - \frac{1}{f^2}\right) = 0. \tag{27}$$

Once the correct real valued and positive root α has been identified, the semi-axes lengths l_{e_j} are given by (3). The eccentricity and the depolarizing factors d_{e_j} of the prototype exterior spheroid are now given by (11) and (12) for the prolate spheroid, or by (14) and (15) for the oblate.

3.3. Sensitivity analysis for high contrast inclusions

A first order Taylor series approximation of the conductivity changes in (18) and (19) is given by

$$\Delta\sigma_j^{\text{eff}} \approx \left.\frac{\mathrm{d}\sigma_j^{\text{eff}}}{\mathrm{d}f}\right|_{f=f_{EI}} \mathrm{d}f, \tag{28}$$

where σ_j^{eff} is given by (6), and where the spherical case (18) is a special case of (19) for which $d_{c_j} = d_{e_j} = 1/3$ and (10) is used. Note that in the spheroidal case

as defined above, the depolarizing factors d_{c_j} and d_{e_j} depend on f via ε.

Assume that the conductivity σ_1 of the inclusion phase is very small and negligible in comparison to the conductivity σ_2 of the exterior phase. The exact expression (6) can then be approximated by

$$\sigma_j^{\text{eff}} \approx \sigma_2 \left(\frac{1 - d_{c_j} + f\left(d_{e_j} - 1\right)}{1 + f d_{e_j} - d_{c_j}}\right). \tag{29}$$

Hence, both σ_j^{eff} and its derivative

$$\frac{\mathrm{d}\sigma_j^{\text{eff}}}{\mathrm{d}f} \approx \sigma_2 \frac{\mathrm{d}}{\mathrm{d}f}\left\{\frac{1 - d_{c_j} + f\left(d_{e_j} - 1\right)}{1 + f d_{e_j} - d_{c_j}}\right\}, \tag{30}$$

are proportional to the complex valued conductivity σ_2 of the exterior medium, and where the constant of proportionality is real valued. In particular, in the spherical case the following simple expressions are obtained

$$\sigma_{\text{sph}}^{\text{eff}} \approx \sigma_2 \left(\frac{2 - 2f}{2 + f}\right), \tag{31}$$

and

$$\frac{\mathrm{d}\sigma_{\text{sph}}^{\text{eff}}}{\mathrm{d}f} \approx -\sigma_2 \frac{6}{(2 + f)^2}. \tag{32}$$

Note that for the a priori effective conductivity σ_{EI} of the inflated lung, (31) yields

$$\sigma_{EI} \approx \sigma_2 \left(\frac{2 - 2f_{EI}}{2 + f_{EI}}\right), \tag{33}$$

which approximates the solution to (17).

By writing $\sigma_2 = \Re\{\sigma_2\}(1 + j\eta)$, and by employing (28) and (30), it is concluded that

$$\Delta\sigma_j^{\text{eff}} \approx \Re\{\Delta\sigma_j^{\text{eff}}\}(1 + j\eta), \tag{34}$$

where η is the loss cotangent associated with the exterior phase having complex valued conductivity σ_2. Note finally that (33) implies that

$$\sigma_{EI} \approx \Re\{\sigma_{EI}\}(1 + j\eta), \tag{35}$$

expressing that the loss cotangent of σ_{EI} is approximately the same as of σ_2.

4. Numerical examples

A theoretical study on the changes in the complex valued conductivity of a lung during tidal breathing is described below. As a prerequisite for this modeling an a priori estimate of the complex valued conductivity σ_{EI} of an inflated lung is needed. Here, the data is taken from [13, Fig. 2e on p. 2257] with $\sigma_{EI} = \sigma_R^a + j\omega\epsilon_0\epsilon_r^a$ where $\sigma_R^a = 0.1\,\text{S/m}$ and $\epsilon_r^a = 2000$ at $200\,\text{kHz}$ yielding $\sigma_{EI} = 0.1\,(1 + j0.22)$. The resulting conductivity of the exterior phase is obtained from (17) and is given by $\sigma_2 = 0.6318\,(1 + j0.22)\,\text{S/m}$. The complex valued conductivity of the air-filled alveoli

is given by $\sigma_1 = \mathrm{j}1.1127 \cdot 10^{-5}\,\mathrm{S/m}$, and which hence can be regarded negligible in comparison to the conductivity σ_2 of the exterior phase.

Another a priori input needed for this modeling is the range of volume fractions $[f_{\mathrm{EE}}, f_{\mathrm{EI}}]$ during tidal breathing. Consider *e.g.*, the lung volume of an adult male with a functional residual capacity of $2.3\,\mathrm{l}$ and tidal volume $0.5\,\mathrm{l}$, *cf.*, [18]. Suppose further that the weight of the two lungs is about $0.8\,\mathrm{kg}$ [19], corresponding approximately to $0.8\,\mathrm{l}$ of blood and tissue. The following volume fractions are then obtained

$$\begin{cases} f_{\mathrm{EE}} = \dfrac{2.3}{2.3 + 0.8} = 0.75, \\[2ex] f_{\mathrm{EI}} = \dfrac{2.8}{2.8 + 0.8} = 0.78, \end{cases} \tag{36}$$

where the results have been rounded to two digits.

The theoretical study based on (18) and (19) (spheres and spheroids) is illustrated in figures 2 through 6 below, where the changes in conductivity are parameterized by the volume fraction $f = f_{\mathrm{EI}} - \Delta f$ with $\Delta f \in [0, 0.03]$ and $f_{\mathrm{EI}} = 0.78$.

In figures 3 and 5 the changes are plotted directly in the complex plane, and it is noted that there is a fixed, almost linear relationship between the changes in the real part of the conductivity $\Re\{\Delta\sigma^{\mathrm{eff}}\}$ and the imaginary part $\Im\{\Delta\sigma^{\mathrm{eff}}\}$. This observation is in full agreement with the theory predicted by the Taylor series approximation (28) and (34) assuming that the changes in volume fraction $\mathrm{d}f = -\Delta f < 0$ are small. Hence, the linear slopes seen in figures 3 and 5 are consistent with the theory predicted by (34) and where $\eta = 0.22$ is the loss cotangent associated with the exterior phase having complex valued conductivity $\sigma_2 = 0.6318\,(1 + \mathrm{j}0.22)$. Note that this loss cotangent is also approximately the same as the one associated with the a priori (effective) background conductivity $\sigma_{\mathrm{EI}} = 0.1\,(1 + \mathrm{j}0.22)$ according to the theory expressed in (35).

As predicted by the linearization theory expressed in (30), the linear slopes seen in figures 3 and 5 are independent of the assumed alveoli model (spherical, prolate spheroidal or oblate spheroidal), as well as of the assumed excitation polarization (excitation aligned along spheroid or orthogonal to it). It is only the magnitude of the conductivity changes that differ in between these different modes of alveolar air-filling and their anisotropy.

In figure 6 is illustrated the different sensitivity slopes that are obtained with a prolate spheroidal alveoli model excitet along its symmetry axis, and with different a priori assumed background conductivities $\sigma_{\mathrm{EI}} = \sigma_{\mathrm{R}}^{\mathrm{a}} + \mathrm{j}\omega\epsilon_0\epsilon_{\mathrm{r}}^{\mathrm{a}}$. As before, the resulting change in complex valued conductivity $\Delta\sigma^{\mathrm{eff}} = \sigma^{\mathrm{eff}}(f) - \sigma^{\mathrm{eff}}(f_{\mathrm{EI}})$ is plotted for volume fractions ranging from $f_{\mathrm{EI}} = 0.78$
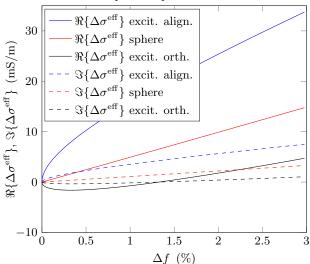

Figure 2. Real and imaginary parts of the change in effective lung conductivity parameter, $\Delta\sigma^{\mathrm{eff}} = \sigma^{\mathrm{eff}}(f) - \sigma^{\mathrm{eff}}(f_{\mathrm{EI}})$, as a function of the change in volume fraction Δf and where the actual volume fraction of alveoli is $f = f_{\mathrm{EI}} - \Delta f$. The plot shows results for a prolate spheroidal alveoli with excitation aligned along and orthogonal to the spheroid, respectively, and which has constant surface area and increasing spheroidal eccentricity (decreasing volume). The plot shows also results for a core sphere with decreasing volume. The exterior Hashin-Shtrikman spheroids (and sphere) have constant volumes and all spheroids are spheres at $f_{\mathrm{EI}} = 0.78$.
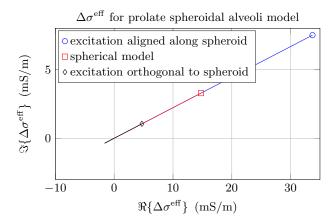

Figure 3. Change in the effective lung conductivity parameter $\Delta\sigma^{\mathrm{eff}}$ from figure 2, plotted here in the complex plane. As in figure 2, the resulting change in complex conductivity $\Delta\sigma^{\mathrm{eff}} = \sigma^{\mathrm{eff}}(f) - \sigma^{\mathrm{eff}}(f_{\mathrm{EI}})$ is plotted for volume fractions ranging from $f_{\mathrm{EI}} = 0.78$ to $f_{\mathrm{EE}} = 0.75$ where the last value at f_{EE} is indicated with the corresponding plot symbol. The plot shows results with a prolate spheroidal alveoli (constant surface area and increasing eccentricity, hence decreasing volume) in comparison with a spherical alveoli (decreasing volume).

to $f_{\mathrm{EE}} = 0.75$ where the last value at f_{EE} is indicated with the corresponding plot symbol. Note that the corresponding changes $\Delta\sigma^{\mathrm{eff}}$ are directly proportional to σ_2 by (30), or σ_{EI} by (33).
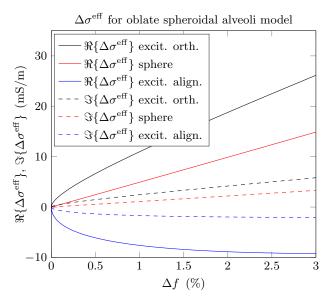
Figure 4. Real and imaginary parts of the change in effective lung conductivity parameter, $\Delta\sigma^{\mathrm{eff}} = \sigma^{\mathrm{eff}}(f) - \sigma^{\mathrm{eff}}(f_{\mathrm{EI}})$, as a function of the change in volume fraction Δf and where the actual volume fraction of alveoli is $f = f_{\mathrm{EI}} - \Delta f$. The plot shows results for an oblate spheroidal alveoli with excitation aligned along and orthogonal to the spheroid, respectively, and which has constant surface area and increasing spheroidal eccentricity (decreasing volume). The plot shows also results for a core sphere with decreasing volume. The exterior Hashin-Shtrikman spheroids (and sphere) have constant volumes and all spheroids are spheres at $f_{\mathrm{EI}} = 0.78$.
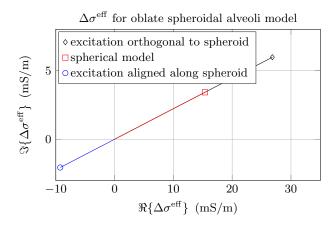

Figure 5. Change in the effective lung conductivity parameter $\Delta\sigma^{\mathrm{eff}}$ from figure 4, plotted here in the complex plane. As in figure 4, the resulting change in complex conductivity $\Delta\sigma^{\mathrm{eff}} = \sigma^{\mathrm{eff}}(f) - \sigma^{\mathrm{eff}}(f_{\mathrm{EI}})$ is plotted for volume fractions ranging from $f_{\mathrm{EI}} = 0.78$ to $f_{\mathrm{EE}} = 0.75$ where the last value at f_{EE} is indicated with the corresponding plot symbol. The plot shows results with an oblate spheroidal alveoli (constant surface area and increasing eccentricity, hence decreasing volume) in comparison with a spherical alveoli (decreasing volume).

5. Summary and conclusions

A theoretical model based on classical homogenization theory and the Hashin-Shtrikman coated ellipsoids has been derived to model the changes in the
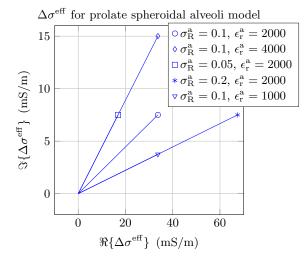

Figure 6. Change in the effective lung conductivity parameter $\Delta\sigma^{\mathrm{eff}}$ for prolate spheroidal alveoli with excitation aligned along the spheroid, as in figures 2 and 3, plotted here for different values of a priori inflated lung parameter $\sigma_{\mathrm{EI}} = \sigma_{\mathrm{R}}^{\mathrm{a}} + \mathrm{j}\omega\epsilon_0\epsilon_{\mathrm{r}}^{\mathrm{a}}$.

complex valued conductivity of a lung during tidal breathing. Here, the alveolar air-filling corresponds to the inclusion phase of the two-phase composite material. The model predicts a linear relationship between the real and the imaginary parts of the changes in the complex valued conductivity of a lung during tidal breathing, and where the loss cotangent of the change is approximately the same as of the effective background conductivity. Hence, even though the magnitude of the change depend on the chosen ellipsoidal model, the loss cotangent of the change is virtually independent of the shape and orientation (anisotropy) of the alveoli. Future work will be aiming to investigate the usefulness of the new model based on experimental and clinical data obtained within the ongoing CRADL study.

Acknowledgments

References

[1] I. Frerichs. Electrical impedance tomography (EIT) in applications related to lung and ventilation: a review of experimental and clinical activities. *Physiological Measurement*, 15(2):1, 2000.

[2] H. R. Carlisle, R. K. Armstrong, P. G. Davis, A. Schibler, I. Frerichs, and D. G. Tingay. Regional distribution of

blood volume within the preterm infant thorax during synchronised mechanical ventilation. *Intensive Care Med*, 36:2101–2108, 2010.

[3] I. Frerichs, M. B. P. Amato, A. H. van Kaam, D. G. Tingay, Z. Zhao, B. Grychtol, M. Bodenstein, H. Gagnon, S. H. Böhm, E. Teschner, O. Stenqvist, T. Mauri, V. Torsani, L. Camporota, A. Schibler, G. K. Wolf, D. Gommers, S. Leonhardt, and A. Adler. Chest electrical impedance tomography examination, data analysis, terminology, clinical use and recommendations: consensus statement of the TRanslational EIT developmeNt stuDy group. *Thorax*, 72:83–93, 2017. doi:10.1136/thoraxjnl-2016-208357.

[4] Erkki Somersalo, Margaret Cheney, and David Isaacson. Existence and uniqueness for electrode models for electric current computed tomography. *SIAM J. Appl. Math.*, 52(4):1023–1040, 1992.

[5] M. Cheney, D. Isaacson, and J. C. Newell. Electrical impedance tomography. *SIAM Review*, 41(1):85–101, 1999.

[6] R. Bayford. Bioimpedance tomography (electrical impedance tomography). *Annu. Rev. Biomed. Eng.*, 8:63–91, 2006.

[7] S. Nordebo, R. Bayford, B. Bengtsson, A. Fhager, M. Gustafsson, P. Hashemzadeh, B. Nilsson, T. Rylander, and T. Sjödén. An adjoint field approach to Fisher information-based sensitivity analysis in electrical impedance tomography. *Inverse Problems*, 26, 2010. 125008.

[8] A. Adler and R. Guardo. Electrical impedance tomography: regularized imaging and contrast detection. *IEEE Transactions on Medical Imaging*, 15(2):170–179, 1996.

[9] A. Adler, J. H. Arnold abd R. Bayford, A. Borsic, B. Brown, P. Dixon, T. J. C. Faes, I. Frerichs, H. Gagnon, Y. Gärber, B. Grychtol, G. Hahn, W. R. B. Lionheart, A. Malik, R. P. Patterson, J. Stocks, A. Tizzard, N. Weiler, and G. K. Wolf. GREIT: a unified approach to 2D linear EIT reconstruction of lung images. *Physiological Measurement*, 30(6):35–55, 2009.

[10] D. Khodadad, S. Nordebo, N. Seifnaraghi, A. D. Waldmann, B. Müller, and R. Bayford. Breath detection using short-time Fourier transform analysis in Electrical Impedance Tomography. In *32nd URSI General Assembly & Scientific Symposium*, pages 2185–2187, Montreal, August 2017.

[11] Margaret Cheney and David Isaacson. Issues in electrical impedance imaging. *IEEE Computational Science & Engineering*, pages 53–62, 1995.

[12] A. Adler, R. Amyot, R. Guardo, J. H. T. Bates, and Y. Berthiaume. Monitoring changes in lung air and liquid volumes with electrical impedance tomography. *Journal of Applied Physiology*, 83(5):1762–1767, 1997.

[13] S. Gabriel, R. W. Lau, and C. Gabriel. The dielectric properties of biological tissues: II. Measurements in the frequency range 10 Hz to 20 GHz. *Phys. Med. Biol.*, 41:2251–2269, 1996.

[14] D. Isaacson, J. L. Mueller, J. C. Newell, and S. Siltanen. Imaging cardiac activity by the D-bar method for electrical impedance tomography. *Physiol. Meas.*, 27:43–50, 2006.

[15] S. J. Hamilton, J. L. Mueller, and M. Alsaker. Incorporating a spatial prior into nonlinear D-bar EIT imaging for complex admittivities. *IEEE Transactions on Medical Imaging*, 36(2):457–466, 2017.

[16] C. Gabriel, S. Gabriel, and E. Corthout. The dielectric properties of biological tissues: I. Literature survey. *Phys. Med. Biol.*, 41:2231–2249, 1996.

[17] S. Gabriel, R. W. Lau, and C. Gabriel. The dielectric properties of biological tissues: III. Parametric models for the dielectric spectrum of tissues. *Phys. Med. Biol.*, 41:2271–2293, 1996.

[18] William F. Ganong. *Review of medical physiology*. Lange Medical Books/McGraw-Hill, New York, 21st edition, 2003.

[19] D. K. Molina and V. J. DiMaio. Normal organ weights in men: part II-the brain, lungs, liver, spleen, and kidneys. *Am J Forensic Med Pathol.*, 33:368–372, 2012.

[20] P. Nopp, E. Rapp, H. Pfützner, H. Nakesch, and C. Ruhsam. Dielectric properties of lung tissue as a function of air content. *Phys. Med. Biol.*, 38:699–716, 1993.

[21] P. Nopp, N. D. Harris, T. X. Zhao, and B. H. Brown. Model for the dielectric properties of human lung tissue against frequency and air content. *Medical & Biological Engineering & Computing*, 35(6):695–702, 1997.

[22] J-R Wang, B-Y Sun, H-X Wang, S Pang, X Xu, and Q Sun. Experimental study of dielectric properties of human lung tissue in vitro. *Journal of Medical and Biological Engineering*, 34(6):598–604, 2014.

[23] Ari Sihvola. *Electromagnetic Mixing Formulae and Applications*. IEE Electromagnetic Waves Series, 47. Institution of Electrical Engineers, 1999.

[24] Graeme W. Milton. *The Theory of Composites*. Cambridge University Press, Cambridge, U.K., 2002.

[25] J. D. Jackson. *Classical Electrodynamics*. John Wiley & Sons, New York, third edition, 1999.

[26] H. M. Nussenzveig. *Causality and dispersion relations*. Academic Press, London, 1972.

[27] F. W. King. *Hilbert transforms vol. I–II*. Cambridge University Press, 2009.

[28] P. M. Morse and H. Feshbach. *Methods of Theoretical Physics*, volume 2. McGraw-Hill, New York, 1953.

[29] C. F. Bohren and D. R. Huffman. *Absorption and Scattering of Light by Small Particles*. John Wiley & Sons, New York, 1983.

[30] J. A. Osborn. Demagnetizing factors of the general ellipsoid. *Phys. Rev.*, 67:351–357, 1945.

[31] D. Zwillinger. *CRC Standard Mathematical Tables and Formulae*. Chapman & Hall/CRC Press LLC, 31st edition, 2003.